7

Noninvasive Imaging of Cardiac Electrophysiology (NICE)

Michael Seger[1], Bernhard Pfeifer[1] and Thomas Berger[2]
[1]*Institute of Electrical, Electronic and Bioengineering, UMIT – The Health and Life Sciences University*
[2]*Division of Internal Medicine III/Cardiology, Medical University Innsbruck Austria*

1. Introduction

1.1 General description and aim of NICE

Many clinically relevant types of cardiac dysfunctions can be diagnosed by a proper knowledge of the spatio-temporal spread of cardiac electrical excitation, such as supraventricular and ventricular tachycardias. This knowledge supports the cardiologist to apply the optimal treatment strategy for the individual patient.

Computer modeling of bioelectric activity has been of interest in cardiac electrophysiology for several decades (Gulrajani R. M., 1988; Johnson J. R., 1997; Modre R. et al., 2001). Additionally, noninvasive imaging of the electrical excitation from recorded electrocardiograms (ECGs) has become a diagnosis tool in clinical electrophysiology (Modre R. et al., 2003; Ramanathan C. et al., 2004). Noninvasive imaging of the electrical function requires the combination of four dimensional anatomical (three dimensions: space) and ECG mapping (one dimension: time) data. This allows computation of the so-called electrocardiographic inverse problem. This means to calculate the unknown sources (e.g., cardiac electrophysiological parameters) by considering the measured – and thus known – anatomical and ECG data in an appropriate manner.

NICE – **N**oninvasive **I**maging of **C**ardiac **E**lectrophysiology – has been developed for investigating and assessing the electrophysiological cardiac status of humans in a noninvasive manner over the past 25 years at Graz Technical University (Graz, Austria), Medical University Innsbruck (Innsbruck, Austria) and UMIT (Hall in Tirol, Austria). Selected publications reflecting the related development and progress of this method are (Berger T. et al., 2006; 2005; 2011; Fischer G. et al., 2000; 1999; Messnarz B., Seger M., Modre R., Fischer G., Hanser F. & Tilg B., 2004; Modre R. et al., 2006; 2003; Pfeifer B. et al., 2008; 2006; Renhardt M. et al., 1992; Seger M. et al., 2004; Tilg B., Hanser F., Modre-Osprian R., Fischer G., Messnarz B., Berger T., Hintringer F., Pachinger O. & Roithinger F. X., 2002; Tilg B. et al., 1992; Wach P. et al., 2001; 1997).

In brief, NICE enables the computation of electrophysiologically and clinically meaningful parameters, such as cardiac activation times (ATs) or the spatio-temporal transmembrane

potential distribution on both the atrial or ventricular surfaces. All the related steps necessary to obtain this information are accomplished exclusively in a noninvasive fashion. Thus

- interventional procedures for diagnostic purposes can be avoided and therefore the risk of complications can be reduced,
- a diagnosis based on the results of NICE can help the cardiologist to plan appropriate therapeutical treatment strategies,
- post-interventional analyses can be performed at higher and more detailed spatial resolutions as compared to the 12-lead standard ECG, and
- patient individual screening or monitoring of changes of electrophysiological behaviour (e.g., CRT) can be performed.

An individual patient-specific model of cardiac electrophysiology gives important information about clinically relevant parameters of atrial and ventricular electroanatomic activation. For this purpose a distinct knowledge of different mathematical, physical and medical disciplines, related methods and applications is essential. The most relevant disciplines involved in NICE are (examples of corresponding activities related to NICE are given in brackets)

- *biomedical signal processing* (filtering, baseline correction and extraction of the relevant portions of the recorded multi-channel ECG signals),
- *biomedical image processing* (segmentation of the patient individual volume conductor model based on medical imaging modalities (e.g., Magnetic Resonance Imaging (MRI)) including heart, chest, lungs, blood masses; registration of the electrodes' positions on the volume conductor model),
- *modelling and simulation of biophysical systems and compounds* (bidomain theory for the biophysical description of the electric sources generated by the myocytes),
- *electrical engineering* (Maxwell's equations applied to describe bioelectrical phenomena and thus to relate the electrical sources to the measured ECG signals),
- *solving techniques applied to inverse problems* (the problem formulation of NICE is ill-posed and requires therefore application of regularization techniques),
- *numerical mathematics* (discretization of the patient's geometry and of the related Maxwell's equations according to the chosen method, e.g., Boundary-Element-Method (BEM), Finite-Element-Method (FEM) or hybride cellular automata based approaches),
- *experimental and clinical electrophysiology* (data analysis, interpretation of the results and implications, future perspectives and possible clinical applications).

2. Methods

2.1 Mathematical/physical background

2.1.1 Description of the problem

The most relevant measures which can be obtained noninvasively are the spatio-temporal distribution of

- epi-, endo- and/or myocardial electrical potentials φ (performed by, e.g., (Ramanathan C. et al., 2004; 2003)),

- transmembrane voltages (difference of intra- and extracellular potentials $\varphi_m = \varphi_{intra} - \varphi_{extra}$; performed by, e.g., (Messnarz B., Tilg B., Modre R., Fischer G. & Hanser F., 2004)) or
- the cardiac activation times τ (time instant when the depolarization of the region of interest occurs; performed by, e.g., (Berger T. et al., 2006; 2011)).

These parameters can be calculated for the outer and inner surfaces of the heart (on the epi- and endocardia) and/or within the myocardium. In case of NICE, the cardiac activation times are determined both on the epi- and endocardia.

The cardiac activation times are related to the ECG on the body surface (also termed Body Surface Potential Mapping – BSPM). Therefore, an appropriate model formulation can be applied. In the following subsections the mathematical derivation for final determination of cardiac activation times $\tau(\mathbf{x})$ (with $\mathbf{x} \in \Omega$ or $\Gamma \subset \mathbb{R}^3$; Γ representing the cardiac surfaces (epi-, endocardia), Ω represents the whole cardiac volume) is presented in a more detailed manner.

2.1.2 Bidomain theory

According to (Geselowitz D. B. & Miller 3rd W. T., 1983) a physical description for the behavior of electrically active tissue – thus also the heart – on a macroscopic scale can be represented by the so-called *bidomain theory*. In Fig. 1 the modeling assumptions for the continuum model

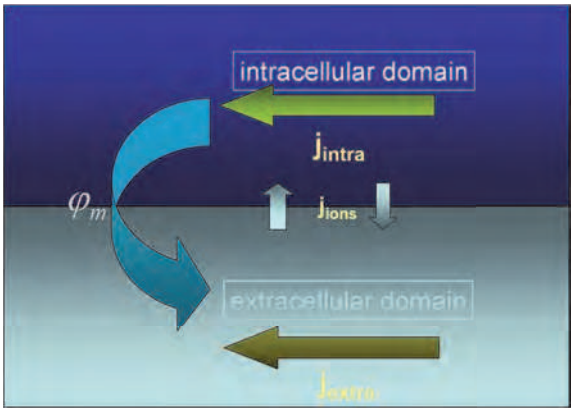

Fig. 1. A schematic snapshot of the intra- and extracellular domain for the *bidomain continuum model* is shown. The intracellular space is separated from the extracellular space by the cellular membrane. Ion currents are able to pass through the membrane via specific ion channels (j_{ions}). Current densities occur within the cell (j_{intra}) and outside the cell in the interstitial space (j_{extra}). The voltage measured as difference between the intracellular and the extracellular potentials is termed transmembrane potential $\varphi_m = \varphi_{intra} - \varphi_{extra}$.

derivating the bidomain theory are shown. As the cardiac fibers (myocytes) are connected to each other via highly conductive *gap-junctions* it is assumed, that intra- and extacellular spaces can be smeared over the whole heart. That means, there is no need to model each cardiac cell individually, but the values necessary to describe the electrical behavior are averaged over a

small tissue volume. As an example, current density j_x in direction of the x-axis can thus be calculated by the intracellular I_{intra} and extracellular I_{extra} current

$$j_x = \frac{I_{intra} + I_{extra}}{\Gamma} = -\frac{\Gamma_{intra}}{\Gamma} \cdot \sigma^*_{intra} \cdot \frac{\partial \varphi_{intra}}{\partial x} - \frac{\Gamma_{extra}}{\Gamma} \cdot \sigma^*_{extra} \cdot \frac{\partial \varphi_{extra}}{\partial x}. \quad (1)$$

The intracellular cross section is denoted by Γ_{intra}, the extracellular by Γ_{extra} and the cross section of the whole cell by Γ. Scalars σ^*_{intra} and σ^*_{extra} represent the conductivities of the intra- and extracellular space, respectively, $\frac{\partial \varphi_{intra}}{\partial x}$ and $\frac{\partial \varphi_{extra}}{\partial x}$ denote the gradients of the corresponding potentials. Combining expressions $\frac{\Gamma_{intra}}{\Gamma} \cdot \boldsymbol{\sigma}^*_{intra}$ to $\boldsymbol{\sigma}_{intra}$, the effective intracellular conductivity, and $\frac{\Gamma_{extra}}{\Gamma} \cdot \boldsymbol{\sigma}^*_{extra}$ to $\boldsymbol{\sigma}_{extra}$, the effective extracellular conductivity, leads finally – for all three Cartesian coordinates – to

$$\boldsymbol{j} = -\boldsymbol{\sigma}_{extra}\mathrm{grad}(\varphi_{extra}) - \boldsymbol{\sigma}_{intra}\mathrm{grad}(\varphi_{intra}). \quad (2)$$

Introducing the transmembrane (or action) potential

$$\varphi_m = \varphi_{intra} - \varphi_{extra} \quad (3)$$

and the bulk conductivity, $\boldsymbol{\kappa}_B = \boldsymbol{\sigma}_{intra} + \boldsymbol{\sigma}_{extra}$, Equation (2) can be reorganized and rewritten to

$$\boldsymbol{j} = -\boldsymbol{\sigma}_{intra}\mathrm{grad}(\varphi_m) - \boldsymbol{\kappa}_B\mathrm{grad}(\varphi_{extra}). \quad (4)$$

Note that bold symbols represent in case of $\boldsymbol{j}$ a vector or in case of e.g., $\boldsymbol{\sigma}_{intra}$ tensors, which means that the electrical conductivities in general can be referred to as electrically anisotropic measures. Applying Equation (16) (the mathematical calculus why the divergence of $\boldsymbol{j}$ is set to zero will be explained in the next subsection 2.1.3), Equation (4) finally results in

$$\mathrm{div}[\boldsymbol{\kappa}_B\mathrm{grad}(\varphi_{extra})] = -\mathrm{div}[\boldsymbol{\sigma}_{intra}\mathrm{grad}(\varphi_m)]. \quad (5)$$

Equation (5) is an elliptical differential equation and also known as BIDOMAIN EQUATION. This equation represents the mathematical model description of electrical cardiac function on a continuum model level. Note, that (5) is – with according change of the values – the same equation as (17) with expression $-\boldsymbol{\sigma}_{intra}\mathrm{grad}(\varphi_m)$ on the right hand side of (5) representing the impressed current density (cardiac electrical source term) $\boldsymbol{j}^{(\mathrm{imp})}$.

The spatio-temporal distribution of φ_m over and within the heart can be most commonly computed by, e.g., cellular automata approaches ((Barbosa C. R. H., 2003; He B. et al., 2002; Hintermüller C. et al., 2004; Saxberg B. E. & Cohen R. J., 1990)). This is of particular interest, when the effects of varying different parameters of the model description on the potentials measured on the torso is the focus of interest, i.e., when solving the forward problem of electrocardiography (see also chapter 2.1.6 describing the forward problem in more detail). When, however, the electrical activation time τ (i.e., the time instant, when the depolarization of the action potential takes place) is of interest, Equation (5) still can be used as the biophysical problem description with a mathematical additional function $\varphi_m(t) = \mathrm{f}(\tau)$ relating the transmembrane potential's shape to the activation time.

2.1.3 Relation of the transmembrane potential φ_m with the (extracellular) potential φ

The general MAXWELL'S EQUATIONS in differential form are:

$$\begin{aligned} \operatorname{div}(\boldsymbol{D}) &= \varrho && \text{Coulomb's law} \\ \operatorname{rot}(\boldsymbol{H}) &= \boldsymbol{j} + \tfrac{\partial \boldsymbol{D}}{\partial t} && \text{Ampere's law} \\ \operatorname{rot}(\boldsymbol{E}) &= -\tfrac{\partial \boldsymbol{B}}{\partial t} && \text{Faraday's law} \\ \operatorname{div}(\boldsymbol{B}) &= 0 && \text{Absence of magnetic monopoles,} \end{aligned} \tag{6}$$

with $\boldsymbol{D}$ describing the electrical displacement, $\boldsymbol{H}$ the magnetic field, $\boldsymbol{E}$ the electrical field, ϱ the electrical charge volume density and $\boldsymbol{j}$ the current surface density. The relations between $\boldsymbol{E}$, $\boldsymbol{D}$ and $\boldsymbol{H}$, $\boldsymbol{B}$ are given by

$$\boldsymbol{D} = \varepsilon \boldsymbol{E} + \boldsymbol{P} \tag{7}$$

$$\boldsymbol{B} = \mu(\boldsymbol{H} + \boldsymbol{M}), \tag{8}$$

where $\boldsymbol{P}$ describes electrical polarization, $\boldsymbol{M}$ magnetization, $\varepsilon = \varepsilon_r \varepsilon_0$ is the electric permittivity, $\mu = \mu_r \mu_0$ is the magnetic permeability. Subscript "r" indicates the relative (matter depending), index "0" the value for the permeability and permittivity of the free space. Finally, with the sum

$$\boldsymbol{j} = \boldsymbol{j}^{(\mathrm{imp})} + \boldsymbol{j}^{(\mathrm{ind})} \tag{9}$$

($\boldsymbol{j}^{(\mathrm{imp})}$ is the vector holding impressed or active currents; $\boldsymbol{j}^{(\mathrm{ind})}$ describes the induced or passive current density) we gain the whole set of equations describing the behavior of electromagnetic fields in matter in the most general form. Equation

$$\boldsymbol{j}^{(\mathrm{ind})} = \boldsymbol{\kappa} \boldsymbol{E} \tag{10}$$

is also termed OHM'S LAW and allows computation of the induced current density applying the electric conductivity tensor $\boldsymbol{\kappa}$.

The following assumptions about modeling electrical function of biological tissue are made:

- Electrical field strengths are not too high $\Rightarrow$ biological tissue is assumed to behave linear with regard to its electrical properties.
- Capacitive as well as inductive effects can be neglected $\Rightarrow$ biological tissue can be described to be purely resistive.
- Due to low frequency components reflecting cardiac electrical activity ($\leqslant$ several kHz) temporal derivatives of Equation (6) can be neglected (quasi-static approximation of Maxwell's equations).

The discussion and justification for the assumptions can be found in, e.g, Geselowitz D. B. (1967); Gulrajani R. M. & Mailloux G. E. (1983); Malmivuo J. & Plonsey R. (1995); Roth B. J. (1991). Applying these assumptions, consequently MAXWELL'S EQUATIONS lead to

$$\mathrm{div}(\boldsymbol{D}) = \varrho \tag{11}$$

$$\mathrm{rot}(\boldsymbol{H}) = \boldsymbol{j} \Rightarrow \mathrm{div}(\boldsymbol{j}) = \mathrm{div}[\mathrm{rot}(\boldsymbol{H})] = 0 \tag{12}$$

$$\mathrm{rot}(\boldsymbol{E}) = 0 \Leftrightarrow \boldsymbol{E} = -\mathrm{grad}(\varphi) \tag{13}$$

$$\mathrm{div}(\boldsymbol{B}) = 0. \tag{14}$$

Consequently, employing (10), Equation (9) can be rewritten as

$$\boldsymbol{j} = \boldsymbol{j}^{(\mathrm{imp})} - \boldsymbol{\kappa}\mathrm{grad}(\varphi) \text{ and with} \tag{15}$$

$$\mathrm{div}(\boldsymbol{j}) = 0 \tag{16}$$

the fundamental equation for biological tissue (with the constraints mentioned above) can be derived:

$$\mathrm{div}[\boldsymbol{\kappa}\mathrm{grad}(\varphi)] = \mathrm{div}(\boldsymbol{j}^{(imp)}). \tag{17}$$

For the special case, that the conductivity $\boldsymbol{\kappa}$ is assumed to be isotropic only, Equation (17) reduces to POISSON'S EQUATION

$$\kappa\Delta(\varphi) = \mathrm{div}(\boldsymbol{j}^{(imp)}), \tag{18}$$

for source-holding domains (i.e., electrically active regions like the heart), whereas for regions having passive properties only (source-free domains), which is reflected by a homogeneous term on the right hand side of Equation (17) leading to LAPLACE'S EQUATION

$$\kappa\Delta(\varphi) = 0. \tag{19}$$

Comparing Equation (17) with (5)

$$\begin{aligned} \mathrm{div}[\boldsymbol{\kappa}\mathrm{grad}(\varphi)] &= \mathrm{div}(\boldsymbol{j}^{(imp)}) \quad \text{with} \\ \mathrm{div}[\boldsymbol{\kappa}_B\mathrm{grad}(\varphi_{extra})] &= -\mathrm{div}[\boldsymbol{\sigma}_{intra}\mathrm{grad}(\varphi_m)] \end{aligned} \tag{20}$$

the following relations of the values between the Maxwell's equations based and the bidomain based derivation can be identified: i) $\boldsymbol{\kappa}_B \leftrightarrow \boldsymbol{\kappa}$, ii) $\varphi_{extra} \leftrightarrow \varphi$, and iii) $-\boldsymbol{\sigma}_{intra}\mathrm{grad}(\varphi_m) \leftrightarrow \boldsymbol{j}^{(imp)}$.

Due to i) the bulk conductivity $\boldsymbol{\kappa}_B = \boldsymbol{\sigma}_{intra} + \boldsymbol{\sigma}_{extra}$ and due to ii) the extracellular potentials φ_{extra} can be interpreted as the passive electrical part, relation iii) reflects the fact, that the impressed currents are due to the intracellular conductivity multiplied by the negative gradient of the transmembrane voltages $\boldsymbol{j}^{(imp)} = -\boldsymbol{\sigma}_{intra}\mathrm{grad}(\varphi_m)$ reflecting the active electrical properties (responsible for generating the action potential in this modelling approach) of the heart.

As a consequence, the extracellular potentials φ_{extra} on the boundary surfaces of the heart are potentials φ, which could be measured, e.g., on the endo- or epicardia by intracardiac

electrodes. In the following the cardiac extracellular potentials will be denoted by φ, the intracellular conductivity tensor by $\boldsymbol{\sigma}_{in}$.

2.1.4 The boundary value problem

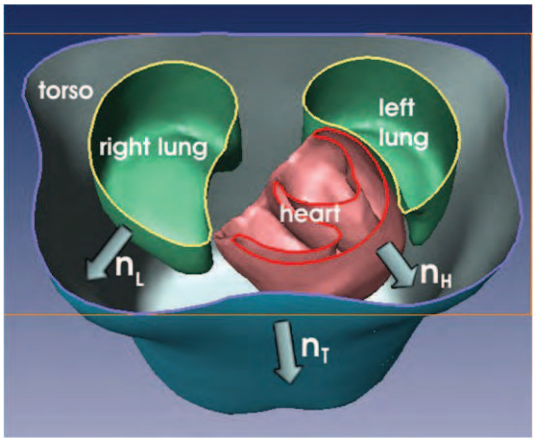

Fig. 2. Cutting plane through the volume conductor model of a patient in antero-oblique view displaying the corresponding boundary surfaces. Vectors $\boldsymbol{n}_{\mathrm{H}}$, $\boldsymbol{n}_{\mathrm{L}}$ and $\boldsymbol{n}_{\mathrm{T}}$ indicate the normal vectors of the related compartment perpendicular to the enclosed volume.

In order to be able to describe bioelectromagnetic phenomena within the human body, all relevant compartments of the volume conductor model (VCM) have to be taken into account. The volume conductor model is a representation of the patient individual geometry comprising the electrically most relevant compartments, which distinguish themselves by their different electrical properties, such as the electrical conductivity (Geselowitz D. B., 1967; Gulrajani R. M. & Mailloux G. E., 1983; Klepfer R. N. et al., 1997; Malmivuo J. & Plonsey R., 1995; Pullan A. J. et al., 2001): heart, bloodmasses within the heart's cavities, left and right lung, and torso. In Fig. 2 a schematic illustration of the boundaries of a volume conductor model is given. The equations

$$\mathrm{div}[\boldsymbol{\sigma}_{bm}\mathrm{grad}(\varphi_{bm})] = 0, \tag{21}$$

$$\mathrm{div}[\boldsymbol{\sigma}_{L}\mathrm{grad}(\varphi_{L})] = 0, \text{ and} \tag{22}$$

$$\mathrm{div}[\boldsymbol{\sigma}_{T}\mathrm{grad}(\varphi_{T})] = 0 \tag{23}$$

form together with Eqation (5) the set of differential equations describing the electrical behavior of each compartment of the volume conductor model, i.e., heart, bloodmasses (abbreviation: *bm*; conductivity $\boldsymbol{\sigma}_{bm}$; not shown in Fig. 2), lungs (*L*; conductivity $\boldsymbol{\sigma}_{L}$), and torso (*T*; conductivity $\boldsymbol{\sigma}_{T}$). Note, that the right hand side of each equation (Eqations (21)–(23)) is 0, as these compartments own electrical passive properties only, hence the impressed current density vanishes.

In order to describe electrical behavior of the whole volume conductor model, boundary conditions have to be taken into account linking the – so far – separate compartments

mathematically together. The following boundary conditions hold on the adjoining compartments' interfaces (termed 1 and 2):

- continuity of the potentials (consequence of Eqation 13)

$$\varphi_1 = \varphi_2 \text{ on intersection of compartments,} \tag{24}$$

  and
- continuity of the current densities perpendicular to the adjoining compartments' interfaces (except torso–outside; consequence of charge conservation):

$$\begin{aligned} \boldsymbol{\sigma}_1 \text{grad}(\varphi_1) \cdot \boldsymbol{n}_1 &= -\boldsymbol{\sigma}_2 \text{grad}(\varphi_2) \cdot \boldsymbol{n}_2 \text{ with} \\ \boldsymbol{n}_1 \cdot \boldsymbol{n}_2 &= -1. \end{aligned} \tag{25}$$

Equation (24) is also referred to as DIRICHLET – the potential is defined – Eqation (25) as NEUMANN BOUNDARY CONDITION, where the gradient of the potential is defined. As the outer surface of the torso is surrounded by air (electrical conductivity $\boldsymbol{\sigma}_{outside} = 0$) the related NEUMANN BOUNDARY CONDITION leads to

$$\boldsymbol{\sigma}_T \text{grad}(\varphi_T) \cdot \boldsymbol{n}_T = 0. \tag{26}$$

For a definite solution of the sought potentials, also a DIRICHLET'S BOUNDARY CONDITION on the torso's surface has to be formulated, as (26) defines only the gradient of the potential. It is advantageous to consider the Wilson central terminal (WCT) for a DIRICHLET'S CONDITION, which in clinical practice defines the zero potential, i.e., the sum of potentials of the right arm (RA), left arm (LA) and left leg (LL) (Fischer G. et al., 2002):

$$\varphi_{RA} + \varphi_{LA} + \varphi_{LL} = 0. \tag{27}$$

2.1.5 Solving the boundary value problem

For solving the sets of Eqation (5)–(23) considering the boundary conditions (24)–(27) to an individual torso geometry, numerical approaches have to be employed. Several numerical methods can be applied, like, e.g., the finite difference, the finite volume, the boundary element (BEM) or the finite element method (FEM). It depends mainly on the intended application, the computational power available and on the basic modeling strategy, which type of numerical solving technique should be used.

In case, that the electrical conductivities of all compartments are modeled to be homogeneous and isotropic, the BEM is the first choice. This approach needs the boundary value problem stated above to be defined in integral from. It has, however, the advantage that only boundary surfaces enclosing a volume of homogeneous isotropic conductivity have to be approximated by, e.g., triangles, whereas using the FEM the whole volume has to be approximated by suitable elements (e.g., tetrahedral elements).

In general and independent from the applied numerical method the equations are transformed into a set of linear algebraic equations by discretization of all compartments of the volume conductor model (e.g., (Fischer G. et al., 2000; Seger M. et al., 2005)). Without loss

of generality the related matrix equation is shown here employing the FEM for the case of tetrahedral elements used for discretization:

$$\boldsymbol{R\Phi} = \boldsymbol{S\Phi_m}. \tag{28}$$

Matrix $\boldsymbol{R}$ is the $(m \times m)$ *left stiffness matrix* (m is the number of tetrahedral nodes of the whole volume) reflecting the properties of the passive compartments, $\boldsymbol{S}$ is the $(m \times s)$ *right stiffness matrix* (s is the number of source nodes), but only a $(s \times s)$ submatrix reflects the active properties of the cardiac tissue (electrically active region) as stated by (5). The passive compartments, (electrical behavior described by Equations (21) – (23)) are represented by zero-entries in $m - s$ rows of $\boldsymbol{S}$. The stiffness matrices are – in case FEM is applied – *symmetric*, *positive semi-definite* and *sparse*, which allows to store only the non-zero entries of the matrices and thus optimizing utilization of computer memory (Press W. H. et al., 2002). The $(m \times t)$ matrix $\boldsymbol{\Phi}$ holds the potentials in all nodes for t time steps, $\boldsymbol{\Phi_m}$ is a $(s \times t)$ matrix consisting of the transmembrane potentials in each (cardiac) source node.

The Wilson central terminal in (27) can be considered by assembling a *terminal-element-matrix* to the global stiffness matrix $\boldsymbol{R}$ employing the potential definition vector $\boldsymbol{w}$ (Fischer G. et al., 2002):

$$\boldsymbol{w}^T\boldsymbol{\Phi} = 0, \qquad \tilde{\boldsymbol{R}} = \boldsymbol{R} + \omega \boldsymbol{w}\boldsymbol{w}^T, \quad \omega > 0. \tag{29}$$

Vector $\boldsymbol{w}$ – the interpolation vector of the torso's surface nodes nearest located to the Wilson terminal electrodes – is *sparse*, as at most three entries (in case of tetrahedral elements) differ from zero. A suitable choice for the positive weighting factor ω is achieved by taking the corresponding pivot elements of $\boldsymbol{R}$ in order to guarantee that entries of $\tilde{\boldsymbol{R}}$ are in the same order of magnitude as $\boldsymbol{R}$. Thus the properties of $\tilde{\boldsymbol{R}}$, i.e., symmetry and sparseness, are conserved. After this manipulation the *positive definite* matrix $\tilde{\boldsymbol{R}}$, can be inverted, yielding for the node potentials of the volume conductor model:

$$\boldsymbol{\Phi} = \tilde{\boldsymbol{R}}^{-1}\boldsymbol{S\Phi_m}, \tag{30}$$

with $\tilde{\boldsymbol{R}}^{-1}\boldsymbol{S}$ representing the *node field matrix*. Introducing the *interpolation matrix* $\boldsymbol{N}$, which relates the e electrode potentials $\boldsymbol{\Phi}_e$ $(e \times t)$ to all node potentials

$$\boldsymbol{\Phi}_e = \boldsymbol{N\Phi} \implies \boldsymbol{\Phi}_e = \boldsymbol{N}\tilde{\boldsymbol{R}}^{-1}\boldsymbol{S\Phi_m}, \tag{31}$$

the *lead field matrix* (or also termed *transfer matrix*) $\boldsymbol{L}$ can be written as

$$\boldsymbol{L} = \boldsymbol{N}\tilde{\boldsymbol{R}}^{-1}\boldsymbol{S}. \tag{32}$$

In case the BEM is applied the discrete formulation, when applying, e.g., linear triangular elements for approximation of the boundary surfaces, the following matrix equation is gained:

$$\boldsymbol{H\Phi} = \boldsymbol{\Phi}_m, \tag{33}$$

where $\boldsymbol{H}$ $(h \times n)$ represents the so-called *double layer matrix*, matrix $\boldsymbol{\Phi}$ $(n \times t)$ contains the potentials in all n boundary surface nodes of the mesh for t time steps and $\boldsymbol{\Phi_m}$ $(h \times t)$ holds the transmembrane potentials in all h source nodes for t time steps. In contrast to the left stiffness

matrix $\boldsymbol{R}$, which occurs in the finite element method, matrix $\boldsymbol{H}$ is dense and rectangular. It is, however, also singular, which is due to the fact, that the potentials on the boundary surfaces of the torso are only determined by NEUMANN'S BOUNDARY CONDITION. Thus, similar to the FEM, a DIRICHLET'S BOUNDARY CONDITION has to be integrated in the double layer matrix $\boldsymbol{H}$. This is done by including a zero-potential definition vector (determined by, e.g., the electrodes comprising the *Wilson-central-terminal*), which is described in detail in (Fischer G. et al., 2002). After this manipulation, matrix $\tilde{\boldsymbol{H}}$ can be inverted employing standard matrix inversion techniques, like, e.g., the Gaussian elimination method, yielding for the potentials $\boldsymbol{\Phi}$ in all nodes of the conductivity interfaces, especially on the torso surface:

$$\boldsymbol{\Phi} = \tilde{\boldsymbol{H}}^{-1}\boldsymbol{\Phi}_m. \tag{34}$$

The computation of the potentials in e electrodes $\boldsymbol{\Phi}_e$ is performed in a similar way as applying the FEM:

$$\boldsymbol{\Phi}_e = \boldsymbol{N}\tilde{\boldsymbol{H}}^{-1}\boldsymbol{\Phi}_m, \tag{35}$$

where the interpolation matrix $\boldsymbol{N}$ ($e \times n$) relates each location of the electrodes to the corresponding nearest boundary surface nodes, and $\boldsymbol{N}\tilde{\boldsymbol{H}}^{-1} = \boldsymbol{L}$ represents the *lead field matrix* computed employing the BEM.

2.1.6 Forward and inverse problem of electrocardiography

The framework elaborated so far can now be employed for two fields:

- the forward (or direct) problem of electrocardiography and
- the inverse problem of electrocardiography.

The forward problem in this context means, that the effect is to be computed which is due to a known cause, in the inverse problem the effect is known and one is seeking for the cause responsible for this effect. In either case a mathematical model based description has to be developed to be able to link effect and cause.

2.1.6.1 Forward problem

For the forward problem this description is the lead field matrix $\boldsymbol{L}$, which represents the mathematical relationship between the electrical cardiac sources $\boldsymbol{\Phi}_{\text{source}}$, e.g., the transmembrane potentials, and the effect $\boldsymbol{\Phi}_{\text{effect}}$, e.g., the potentials measured by the electrodes:

$$\boldsymbol{\Phi}_{\text{effect}} = \boldsymbol{L}\boldsymbol{\Phi}_{\text{source}}. \tag{36}$$

Thus – when the sources are assumed to be the transmembrane potentials – solving the forward problem of electrocardiography is possible for individual heart, lungs and torso geometries (computation of the lead field matrix by means of the above described methods) when also the spatio-temporal distribution of the transmembrane potentials is known. The transmembrane potential distribution can be computed by, e.g., a cellular automaton taking various properties depending on different cardiac tissue types into account (Barbosa C. R. H., 2003; He B. et al., 2002; Modre R. et al., 2006).

Apart from the transmembrane potential source formulation, other electrical cardiac source formulations are employed: the so-called epicardial potential (more precisely: pericardial) (Greensite F. & Huiskamp G., 1998; Ramanathan C. et al., 2004). In the epicardial potential formulation the potentials on the heart surface (i.e., on the epicardial surface only) are modeled to be electrical sources, which means, that – with respect to the bidomain theory – only extracellular potentials have to be taken into account for solving the forward problem. This formulation can be extended geometrically to the whole heart surface formulation, where not only the epicardial but also the endocardial extracellular potential distribution is modeled as electrical cardiac source. The major problem, however, employing these two latter methods in the forward modeling is the fact, that computing the potentials on the body surface requires knowledge of the potential distribution on the heart surfaces, which cannot directly be linked to the cardiac action potentials. Therefore, most commonly current dipoles are used in order to represent cardiac electrical activation.

2.1.6.2 Inverse problem

The computation of an underlying source leading to an observed and measured effect requires the knowledge of the relationship between source and effect and available data representing the effect. The mathematical relationship is established by the lead field matrix $\boldsymbol{L}$, the measured data reflecting the effect is represented by the matrix $\boldsymbol{\Phi}_{\text{effect}}$ in (36). It is, however, not straightforward to compute the sources by simply inverting the lead field matrix $\boldsymbol{L}$ in (36). This is due to the fact that the inverse problem of electrocardiography is ill posed, which means, that at least one of the following conditions (HADAMARD'S DEFINITION of well posedness) is broken:

- for all admissible (source) data a solution exists,
- for all admissible (source) data the solution is unique and
- the solution depends continuously on the (source) data.

In case of the inverse electrocardiographic problem at least the two last criteria are not fulfilled. Thus, in general, the inverse solution is neither unique nor continuously depending on the data. Therefore methods have to be applied which deliver a reasonable source distribution $\boldsymbol{\Phi}_{\text{source}}$, like, e.g., *regularization techniques*. Regularizing means in this context to impose constraints onto the electrical sources in question and thus to confine the solution space. The effect in terms of computing the cardiac activation sequence is, that only physiologically meaningful epi- and endocardial breakthroughs are allowed to occur (spatial regularization). The regularization is controlled by a regularization parameter, which has to be determined in order to achieve an optimal distribution of the cardiac sources.

An even stricter confinement of the solution space can be achieved by incorporating a-priori information about essential physiological properties of the transmembrane potential (temporal regularization). In the following, only one inverse approach is described in more detail as this method is the one used in NICE. It is not intended to reflect the entire spectrum of inverse algorithms employed in the field of electrophysiology, as this is far beyond the focus of this chapter. A detailed elaboration about inverse problems in general can be found, e.g., in (Engl H. W. et al., 1996).

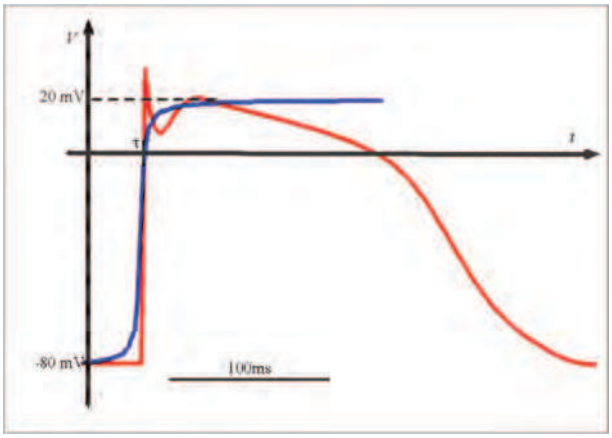

Fig. 3. Measured action potential (red) of a ventricular myocyte (mid-myocardial cell) and the corresponding time course of an approximated one (blue) employing Equation (37). Parameter τ represents the related activation time.

Activation time imaging – Noninvasive imaging of cardiac electrical function – NICE

The transmembrane potential's shape is described by an arctan-like-function (see Fig. 3). The transmembrane potential denoted by φ_m can be approximated by

$$\varphi_m(\tau, t) = \frac{u}{2}\left\{1 + \frac{2}{\pi}\text{atan}\left[\pi\frac{t-\tau}{w}\right]\right\} + a, \tag{37}$$

where $\varphi_m(\tau, t)$ is computed at each source point on the cardiac surface with the parameters resting membrane potential a (a value of $= 0.09$ V has been used in our computations), action potential amplitude u ($= 0.1$ V), rise time w ($= 2 \cdot 10^{-3}$ s) and activation time τ. Equation (37) is an approximation of the time course of the action potential, but it has the advantage, that the number of parameters to be determined in the inverse computation is reduced to only one: the activation time.

The functional to be minimized with respect to τ is (Modre R. et al., 2001; 2002)

$$\|\boldsymbol{L}\Phi_m - \boldsymbol{D}\|_F^2 + \lambda^2\|\Delta\tau\|_2^2 \longrightarrow \text{ min.} \tag{38}$$

The *surface Laplacian* Δ (Huiskamp G. J., 1991) in (38) represents the regularization term and is introduced in order to avoid an unphysiological activation pattern by smoothing the solution of the activation time map. Parameter λ determines the amount of regularization and is calculated employing the L-curve method (Hansen P. C., 2001), weighting the residual norm on the left hand side of (38) against the spatial regularization term leading to an L-shaped curve. The optimal solution is said to be found, when the curve exposes the corner of the L-shape. As the relationship between matrix $\boldsymbol{D}$ with the dimensions (number of electrodes $\times$ depolarization time instants) contains the measured ECG data in the electrodes and $\|\cdot\|_F$ represents the FROBENIUS' NORM. activation time and transmembrane potential is non-linear, the resulting problem to be solved is an ill-posed, non-linear, inverse problem and requires,

e.g., a quasi-Newton-method to be properly solved. As a starting vector for the solution to be searched for the result of the *critical point theorem* is employed (Huiskamp G. & Greensite F., 1997).

The numerical solution was based on the Boundary Element Method with the chosen electrical (isotropic) conductivity values for each compartment:

- heart:
  - effective intracellular conductivity: 0.1 Sm^{-1}
  - bulk conductivity: 0.2 Sm^{-1} (i.e. the sum of effective intra- and extracellular conductivity according to the bidomain model)
- lungs: 0.08 Sm^{-1}
- cavitary blood masses: 0.6 Sm^{-1}
- chest: 0.2 Sm^{-1}

The non-linear problem can be solved by a sequence of linearised ill-posed problems(Modre R. et al., 2001).

A computationally optimized and slightly different approach for solving the inverse problem in terms of computing the cardiac activation times can be found in (Fischer G., Pfeifer B., Seger M., Hintermüller C., Hanser F., Modre R., Tilg B., Trieb T., Kremser C., Roithinger F. X. & Hintringer F., 2005). The major differences are, that a sigmoidal function as template function for the transmembrane potential is applied and the regularization strategy for finding the optimal inverse solution is not based on the L-curve method but on starting with a high value for the regularization parameter λ, and successively using the resulting activation time map for the next iterative computation with a reduced value of λ. This procedure is repeated until λ is set to zero in the last step and the final computed activation time map is regarded as the solution to the ill-posed inverse problem.

2.2 Clinical background

In clinical routine the diagnosis of cardiac arrhythmias, infarction or related disorders is based on the standard 12-lead ECG. The interpretation of the standard ECG by the cardiologist allows in general to obtain a clinical diagnosis using a rough measure of the heart's electrophysiological properties. The surface ECG lacks precise geometrical information of the underlying spatiotemporal electroanatomical substrate. If a more accurate or detailed information about the electroanatomical activation of the heart can be obtained (e.g., the localization of an accessory pathway situated on the ventricles' basis) a more detailed or appropriate procedure can be applied. Up to date, this information can be obtained by an invasive procedure with a catheter and – in most of the cases – an electro-anatomic mapping system (e.g., CARTO™ (Biosense Webster, Inc.)) in an electrophysiology laboratory, which is, however, linked to some risks for the patient due to the intervention. Therefore, it would be favourable to determine relevant cardiac electrophysiological parameters in a fully noninvasive fashion.

A relevant parameter for diagnosis of cardiac arrhythmias is the cardiac activation time. A cardiac activation time map on the epi-, endo- and myocardium enables to, e.g.,

- determine of the origin of cardiac focal events (e.g., atrial and ventricular ectopies, accessory pathways),
- localize scar tissue (e.g, ischemic heart disease)
- determine macroreentry based tachycardias (e.g., atrial flutter)
- discover the starting point and/or rotor evolution of atrial fibrillation,
- plan interventional procedures (electrophysiology study (EPS), pacemaker or implantable cardioverter defibrillator (ICD) implantatations, cardiac resynchronization therapy (CRT)).

An additional benefit of NICE is the fact that it does not rely on stable arrhythmias. NICE allows single-beat calculation of electroanatomical activation of the heart. This is, for several reasons, of special clinical interest as many arrhythmias do not show stable activation patterns.

The activation time map represents the spatio-temporal spread of electrical excitation (i.e., the progression of the action potential's depolarization phase) for epi/endocardial as well as for midmyocardial tissue and has the property to offer detailed information with sufficient geometrical accuracy for further diagnostic and therapeutical interventions.

2.3 NICE – Workflow definition – technical background

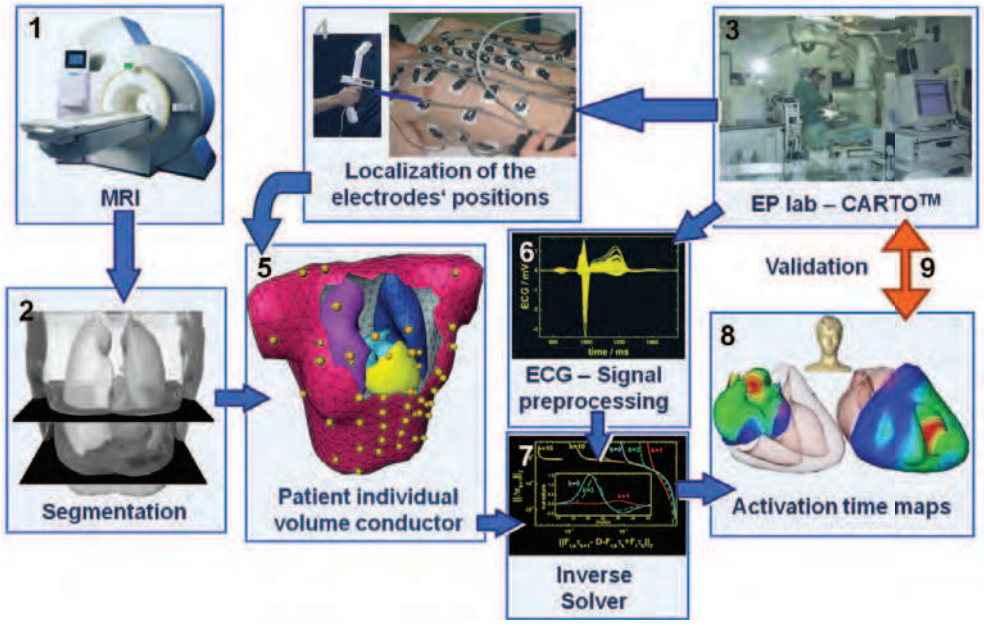

Fig. 4. The workflow scetch as applied for NICE during the validation studies performed in the electrophysiology lab. The sequences are indicated by numbers 1 – 9. For a detailed description of the workflow please refer to the text.

The workflow which was applied for the clinical validation studies (see also section 3.1) is depicted in Fig. 4. The workflow for the results given in section 3.2 and 3.3 (cardiac resynchronization therapy) is shown in Fig. 4. For all studies presented in this chapter written

informed consent of the patients was acquired. All studies were approved by the local ethics committee.

2.3.1 Magnetic resonance imaging, segmentation and the patient individual volume conductor model (steps 1, 2 and 5 in Fig. 4)

For generation of the patient individual volume conductor model the anatomy of the patient has to be acquired.

To create a volume conductor model in order to estimate the electrical spread in the human heart, those compartments need to be considered, which show to have a major influence on the bioelectrical properties (Bradley C. et al., 2000). With respect to NICE these compartments are:

- chest (medium electrical conductivity, surface electrodes),
- lungs (low electrical conductivity, filled with air),
- atrial and ventricular blood masses (high electrical conductivity),
- atrial and ventricular myocardium (medium electrical conductivity, electrical sources).

The image acquisition was performed by MRI using a Magnetom-Vision-Plus 1.5 T (Siemens Medical Solutions) scanner. The atrial and ventricular geometry was recorded in CINE-mode during breath-hold (expiration, short-axis scans, 4 – 6 mm spacing). The shapes of the lungs and the torso were recorded in T1-Flash-mode during breath-hold (expiration, long-axis scans, 10 mm spacing).

For localization and coupling of the mapping electrodes vitamin E capsules were used. These markers are clearly visible within the MRI images and can therefore be easily identified. Seven markers (anatomical landmarks on the anterior and lateral chest wall) were used to couple the locations of the electrodes to the MRI frame. Eleven capsules were attached on the back, in order to tag the positions of the posterior electrodes, which were not accessible during the electrophysiology study. A volume conductor model with electrode positions visualized by spheres is depicted in Fig. 5. The next step was the volume conductor modeling task using two volume data sets. The short-axis data was used for modeling intracardiac blood masses, the ventricles' myocardium and the atria. The axial data set was used for modeling the lungs and chest surface.

Due to the variety of the different compartments the volume conductor model requires different compartment-specific approaches as there is no uniform segmentation approach capable of extracting different compartments (Pfeifer B. et al., 2005; 2008; 2006; 2007). Furthermore, there are two pre-processed data sets (short-axis scan and axial scan) to handle this modeling task.

To meet these requirements, the Medical Segmentation Toolkit (MST) was developed (Pfeifer B. et al., 2005; 2008; 2006). The Medical Segmentation Toolkit enables an easy integration of a variety of state-of-the-art frameworks and segmentation methods. The framework facilitates the development of segmentation pipelines to extract different compartments semiautomatically after initial parameter settings. After extraction the compartments were coupled together to the volume conductor model. This modeling part

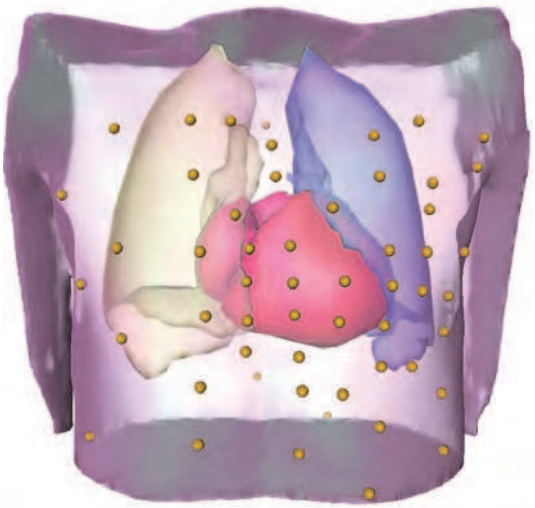

Fig. 5. Volume conductor model generated from 3-D cine MRI data with two axial MR scans with overlaid electrode positions (yellow spheres) in an anterior-posterior view. The thorax and the left (blue) and right (yellow) lungs are displayed in transparent style. Parts of the atria (velvet) are hidden by the ventricles (red).

needed to be done in a short time period because the time between the MRI procedure and the catheter intervention was normally limited by two hours. In clinical routine this time interval should be as short as possible to allow "online" data acquisition (i.e., computation of the cardiac electrical activation times directly at the catheter laboratory) (Seger M. et al., 2004).

2.3.2 Electrophysiology lab, localization of electrode position (steps 3, 4 and 6 in Fig. 4)

The Mark-8 body surface potential mapping system (Biosemi V. O. F.) is an online portable computer acquisition system with data transmission by optical fibre (SippensGroenewegen A. et al., 1998; Tilg B., Hanser F., Modre-Osprian R., Fischer G., Messnarz B., Berger T., Hintringer F., Pachinger O. & Roithinger F. X., 2002). Electrode signals are amplified and AD converted with a 16-bit converter at a sample rate of 2,048 Hz per channel. A radiotransparent carbon electrode array (University of Amsterdam, The Netherlands) was used to record unipolar ECG data from 62 torso sites (anterior chest: 41; posterior chest: 21). The Wilson central terminal defined the reference potential. The positions of the anterior and lateral electrodes and of the seven anterior reference (sternum, left and right rib cage) landmarks were digitized employing the FASTRAK® digitizing system (Polhemus, Inc.). The same seven markers were also digitized with the CARTO™ system, providing coordinate transformation of the invasively obtained data to the MRI frame. The derived ECG signals were then pre-filtered , baseline corrected and the necessary portions of the ECGs (i. e., P-wave for reconstruction of atrial, QRS-complex for reconstruction of ventricular activation times) were extracted employing a self developed software framework implemented in MATLAB® (The MathWorks, Inc.) based on the investigation of the root mean square (RMS) of all

non-corrupted channels of the recorded ECG signals (Berger T. et al., 2006; 2011). Channels were excluded if their signal to noise ratio was low or when electrodes could not be attached to the patient's chest due to medical reasons (e.g., electrode's position at the implant site of the pacemaker).

2.3.3 Computation of the activation time imaging map and validation (steps 7, 8 and 9 in Fig. 4)

Cardiac activation time maps were computed employing inverse solvers (Fischer G., Hanser F., Pfeifer B., Seger M., Hintermüller C., Modre R., Tilg B., Trieb T., Berger T., Roithinger F. X. & Hintringer F., 2005; Modre R. et al., 2001). Electrically isotropic conductivities were assumed for all compartments of the volume conductor model (therefore the boundary element method was applied for computing the lead field matrix). According to previous data (Modre R. et al., 2006) this is a justified assumption also for the cardiac intra- and extracellular conductivities having neglectable influence on the solution of the inverse problem for determining cardiac activation times.

For example, NICE allows the cardiologist to localize the insertion site of an accessory pathway prior to invasive intervention (e.g., Wolff-Parkinson-White (WPW) Syndrome) (Berger T. et al., 2006; Modre R. et al., 2001; 2002; Tilg B., Fischer G., Modre R., Hanser F., Messnarz B., Schocke M., Kremser C., Berger T., Hintringer F. & Roithinger F. X., 2002). Using radiofrequency ablation the insertion site of the accessory pathway was disconnected (Morady F., 1999). After this, the successful ablation site within the CARTO™ map was used for validation of the NICE derived insertion site of the accessory pathway (Berger T. et al., 2006).

3. Results

NICE enables the visualization of atrial and ventricular electroanatomical activation (Berger T. et al., 2006; Modre R. et al., 2003). NICE was validated by comparing the electroanatomic activation sequences with data obtained by invasive electroanatomical mapping (CARTO™). Thus, a quantitative estimation of the mean localization error of NICE was performed. The corresponding findings are shown in the first part of the results' section. Assessment of cardiac resynchronization therapy has been the second major focus of future applications of NICE in clinical electrophysiology and will be described in the second part of the results' section. In the third part first preleminary results of the activation time map of a newly developed pacemaker device are presented.

3.1 Electrophysiology laboratory – validation of NICE

Modre et al. (Modre R. et al., 2003) tested the hypothesis that human atrial activation time imaging is feasible with sufficient spatial and temporal resolution. For the first time, noninvasive atrial activation time imaging was performed in a clinical environment and validated with electroanatomic mapping, invasively localized pacing sites, and pacing at anatomic markers (e.g., pulmonary veins). One example of the results of this study is given in Fig. 6 for activation time imaging of sinus rhythm and in Fig. 7 showing the activation time map for pacing within the right atrial appendage. The activation time map on the

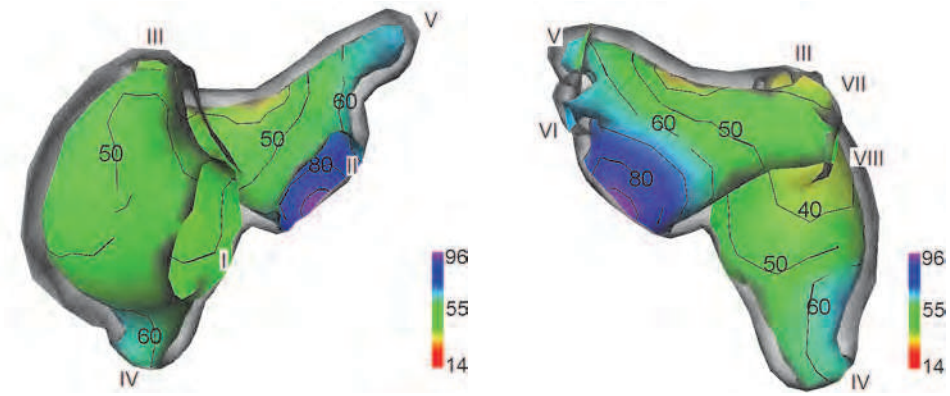

Fig. 6. Atrial endocardial activation time map for sinus rhythm. The isochrones (given in ms) are displayed in intervals of 10 ms, the numbers at the color maps represent ms. Left panel displays the atria in a anterior-posterior, right panel in a posterior-anterior view. The epicardia are displayed in transparent style. Roman numbers indicating anatomical locations of: I. . . tricuspid annulus; II. . . mitral annulus; III. . . vena cava superior; IV. . . vena cava inferior; V. . . left upper pulmonary vein; VI. . . left lower pulmonary vein; VII. . . right upper pulmonary vein; VIII. . . right lower pulmonary vein.

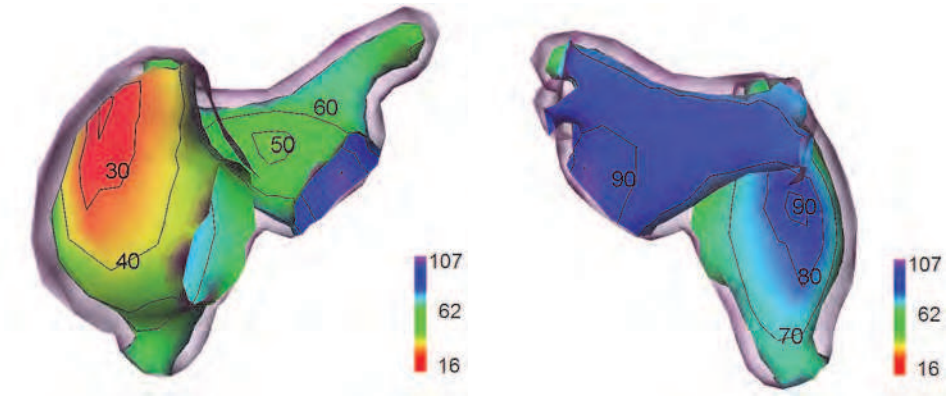

Fig. 7. Atrial endocardial activation time map for pacing in the right atrial appendage. The isochrones (given in ms) are displayed in intervals of 10 ms, the numbers at the color maps represent ms. Left panel displays the atria in a anterior-posterior, right panel in a posterior-anterior view. The epicardia are displayed in transparent style.

endocardium for pacing within the right atrial appendage of the right atrium shows one breakthrough point at the high right atrium close to the breakthrough point on the epicardium at 20 msec. In the right atrium, activation propagated from the high right atrium to the inferior vena cava and the superior vena cava. Finally, the posterior wall of the right atrium was activated 90 msec after pacing. Depolarization ofthe left atrium started 50 msec after the pacing spike. The latest activation of the atria was found at the posterior wall of the left atrium near the mitral annulus 100 msec after pacing. The individual complex anatomic model of the

atria of each patient in combination with high-quality mesh optimization and precise data coupling enabled accurate activation time imaging, resulting in a localization error for the estimated pacing sites of 10 mm in the worst case. (Modre R. et al., 2003)

The aim of the study by Berger et al. (Berger T. et al., 2006) was to test the hypothesis that noninvasive ventricular activation mapping was feasible in the clinical setting of a catheter laboratory with sufficient spatial and temporal resolution. For the first time, noninvasive mapping of human ventricular pre-excitation was performed and the results were validated by invasive 3-D electroanatomic mapping (CARTO™).

Seven patients (3 female; mean age 29 $\pm$ 9 years) with overt ventricular pre-excitation underwent electrophysiologic examination and subsequent radiofrequency catheter ablation of the accessory pathway. All patients had structurally normal hearts which was confirmed by prior transthoracic echocardiography.

The reconstructed activation time maps of ventricular pre-excitation were validated with the catheter-based electroanatomic data (CARTO™) and anatomical markers. For quantitative analysis, the ablation site positions were digitized and coupled with the computer model as described in (Modre R. et al., 2003; Tilg B., Fischer G., Modre R., Hanser F., Messnarz B., Schocke M., Kremser C., Berger T., Hintringer F. & Roithinger F. X., 2002). The last (successful) ablation site was used to calculate the spatial and temporal accuracy of NICE. The position error of the NICE-based activation mapping was defined as the distance between the site of earliest activation on the reconstructed NICE map and the successful ablation site on the CARTO™ map. The color coded activation time maps of three patients of this study is shown in Fig. 8.
The root mean square (RMS) distances between the computed location of the accessory pathway insertion site and the successful ablation sites for all seven patients were 18.7 $\pm$ 5.8 mm for normal AV conduction and 18.7 $\pm$ 6.4 mm during adenosine-induced block. These results have to be interpreted carefully with special attention to the fact of the dispersion of ablation sites during clinical routine. For quantification of this measure the RMS distance between the unsuccessful ablation sites and the localization of successful radiofrequency application was computed, which was found to be 14 $\pm$ 5 mm for all seven patients. Moreover, conventional radiofrequency ablation catheters create lesions with an estimated size of 5 to 8 mm (Simmons W. N. et al., 1996). Taking these circumstances into account, the localization of the accessory pathways' insertion sites computed by NICE showed a strong concordance with the invasively determined successful ablation sites. (Berger T. et al., 2006)

3.2 Cardiac resynchronization therapy

Cardiac resynchronization therapy (CRT) has developed as an established treatment of patients with severe heart failure refractory to optimal medical therapy. Large clinical trials showed a significant benefit on mortality and on morbidity in patients with wide QRS complex in NYHA class III and severely impaired left ventricular ejection fraction (LVEF) (Cleland J. G. et al., 2005).

In CRT a pacemaker or an ICD device is implanted and resynchronization of the ventricles is achieved by a synchronization of the timing of both left and right ventricular pacing (biventricular pacing). The right ventricular pacing electrode is in general placed in the right

ventricular apical region. The left ventricular pacing electrode is positioned in the left lateral ventricular free wall. This electrode position can be achieved by placement of the electrode via the coronary sinus and coronary veins.

In a previous study we were able to visualize biventricular endocardial and epicardial activation in heart failure patients who underwent CRT. These activation sequences were compared to the activation sequences of a healthy control group by using NICE (Berger T. et al., 2011).

Ten patients (1 female, mean age 63 $\pm$ 6 years, NYHA class III and class IV, LVEF $<$ 35 %) with congestive heart failure (ischemic n = 2) and left bundle branch block (LBBB) undergoing CRT and ten patients (4 females; mean age 31 $\pm$ 16 years, LVEF $>$ 50 %) without structural heart disease and normal atrioventricular conduction undergoing an electrophysiology study (control) were included in the study. An ECG butterfly plot of 65 channels of one patient of this study is depicted in Fig. 9 for native (blue) rhythm and for biventricular paced rhythm (red). The dotted vertical lines indicate the extracted QRS-intervals for native rhythm and for biventricular pacing.

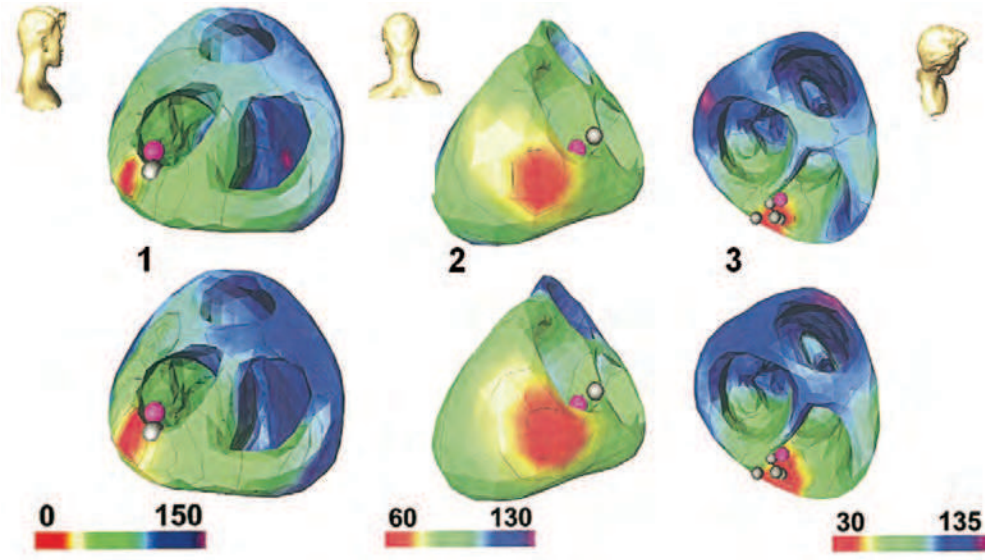

Fig. 8. The location of earliest ventricular activation as computed by NICE is indicated in red. The ablation points are denoted by grey markers, and the location of successful ablation is given by a purple marker, indicating the ventricular insertion site of the accessory pathway. Upper panels show activation sequences during normal atrioventricular (AV) conduction, lower panels show activation sequences during adenosine-induced AV block. Head icons indicate point of view. Red color indicates early, blue–velvet color late electrical activation (see also the colormaps at the bottom with the related activation times in ms).
From (Berger T. et al., 2006) with modification.

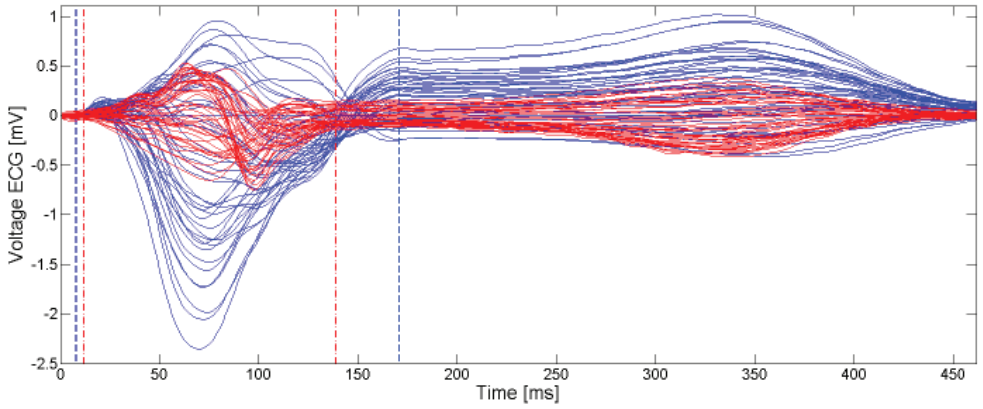

Fig. 9. Butterfly plot of the ECG of the 65-body surface ECG leads during native sinus rhythm (blue) and biventricular pacing (red) of one patient who participated in a CRT-study. The dotted vertical lines indicate begin and end of the QRS complex. From (Berger T. et al., 2011).

The activation time maps for a patient with left bundle branch block (LBBB) is shown in Fig. 10 for native rhythm (left upper panel), right ventricular pacing (RV pacing; right upper panel), left ventricular pacing (LV pacing; left lower panel) and biventricular pacing (right lower panel). The QRS durations clearly indicate an improvement by biventricular pacing as compared to the native rhythm, which could also be confirmed by the activation time maps. There is obviously a high correlation between the intrinsic activation map of a LBBB patient and the activation time map of a control patient during RV pacing. This finding can be related to the fact that in a patient with LBBB the electrical activation starts within the right ventricle and the left ventricle is activated with a temporal delay. This typical activation pattern is similar to the activation pattern during RV pacing. (Berger T. et al., 2011)

The endo-, epicardial and septal breakthrough times in the left and right ventricles could also be determined using NICE. The corresponding times for the LBBB patients and the control group are depicted in Table 1. NICE revealed significant differences between the control and the LBBB patient cohort which is in concordance with previous results (Rodriguez L. M. et al., 2003).

3.3 NICE applied to a CRT patient with novel quadripolar LV pacing lead

New developments in electrode design allows more sophisticated options in stimulation of the left ventricle. One of these new devices uses a left-ventricular pacing lead with four distinct electrodes (VectSelect Quartet™, St. Jude Medical). The activation time maps for both the left and the right ventricle using different LV pacing vectors were investigated noninvasively by NICE. This new technique allows selecting between 10 different pacing vectors by combination of the LV electrodes and the RV coil. The implanted leads are displayed in Fig. 11 acquired by fluoroscopy after succesful CRT implantation.

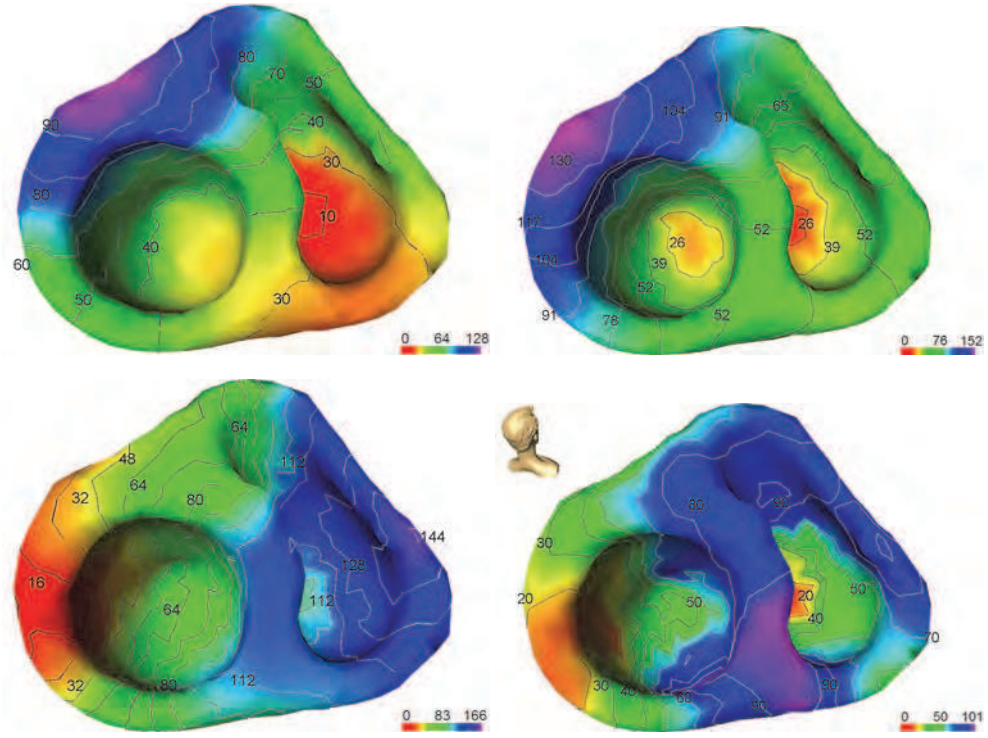

Fig. 10. Activation time maps (isochrones given in ms after first onset of depolarization) showing the left and the right ventricles of a patient with left bundle branch block who underwent CRT in a cranial view (note the head icon indicating the spatial orientation). Left upper panel depicts the activation time map due to native rhythm, right upper panel shows the activation time map during RV pacing, lower left panel shows the activation time map during LV pacing, lower right panel during biventricular pacing. Red color indicates early electrical activation, velvet color indicates areas of late electrial activation. The corresponding QRS durations were: native rhythm: 128 ms; RV pacing: 152 ms; LV pacing: 166 ms; bivent pacing: 101 ms. Note the different scaling of the colormaps for each of the four activation time maps.

The activation time maps determined by NICE are depicted in Fig. 12 for two selected left ventricular pacing sites:

- lead 1 (Distal 1) to lead 2 (Mid 2) defined as pacing vector 1, and
- lead 4 (Proximal 4) to RV coil defined as pacing vector 10

(see Fig. 11 for the locations of the related pacing leads in the 2-D fluoroscopic picture).

	right ventricle			left ventricle		
	endo [ms]	epi [ms]	septal [ms]	endo [ms]	epi [ms]	septal [ms]
control intrinsic	$12 \pm 13^{*}$	$19 \pm 13^{*}$	$20 \pm 10^{*}$	$17 \pm 10^{*}$†	$24 \pm 16^{*}$†	$16 \pm 10^{*}$†
control RV pacing	$0 \pm 1^{*}$	$14 \pm 6^{*}$	$12 \pm 11^{*}$	$41 \pm 13^{*}$	$36 \pm 16^{*}$	$34 \pm 11^{*}$
LBBB intrinsic	7 ± 10†	10 ± 8†	17 ± 12†	46 ± 19†‡	49 ± 16†‡	36 ± 13†
LBBB RV pacing	0 ± 0†‡	15 ± 6‡	16 ± 6‡	50 ± 18§	51 ± 17§	37 ± 10
LBBB biventricular pacing	16 ± 13‡	28 ± 12†‡	30 ± 11†‡	17 ± 7‡§	1 ± 2‡§	40 ± 11

Table 1. Endocardial and epicardial left- and right ventricular breakthrough times in milliseconds after QRS-onset (0 ms) during intrinsic rhythm and different pacing modes of control group versus LBBB patients. Symbols '*', '†', '‡', and '§' represent a significant column-wise difference (p-value < 0.05) between the corresponding different pacing procedures and rhyhtms. From (Berger T. et al., 2011).

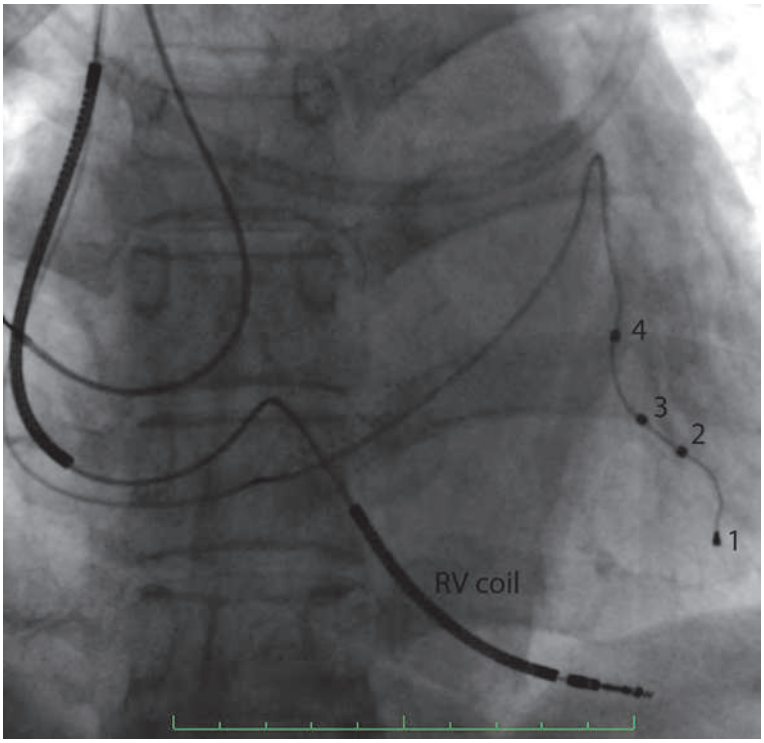

Fig. 11. 2-D picture showing the leads of the Promote Quadra™ device (St. Jude Medical) acquired by fluoroscopy in an anterior-posterior view. The four electrodes on the left ventricular lead (inserted via the coronary sinus) are clearly visible in this picture. The numbers indicate the postion of the distinct electrodes of the left lead. The RV coil is located in the right ventricle and is also part of some of the possible stimulation vectors.

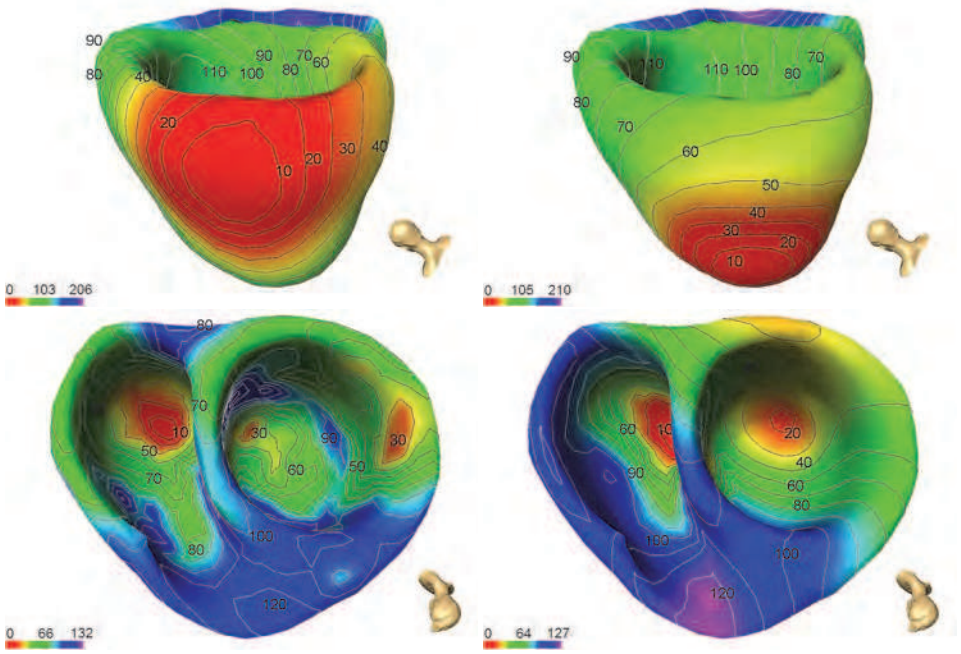

Fig. 12. Activation time maps for left ventricular pacing only (upper panels) and pacing in the right ventricular apex and at the left ventricular lateral wall (lower panels). Note the head icon for spatial orientation. For both figures on the left hand side left ventricular pacing was performed with pacing vector 10 (Proximal 4 to RV coil; see Fig. 11 for the related leads' positions), the figures on the right hand side show the results for left ventricular pacing employing vector 1 (Distal 1 to Mid 2).

4. Discussion and conclusion

NICE allows to determine the electrical activation times in a fully noninvasive fashion by combining 3-D geometrical data (acquired by MRI, CT, ultrasound etc.) with a high-resolution multi-channel ECG recording system. As the problem is ill-posed regularization has to be applied. In case of NICE for regularization in the time domain an arcus-tangens-function is introduced in order to mimick the depolarization sequence of a myocyte. Geometrial regularization is achieved by a 2nd order Tikhonov regularization applying the surface Laplacian.

Studies confirmed that NICE can be applied in a clinical environment for solving electrophysiologically relevant problems (Berger T. et al., 2006; 2005; 2011; Modre R. et al., 2004; 2003; Seger M. et al., 2004; Tilg B., Hanser F., Modre-Osprian R., Fischer G., Messnarz B., Berger T., Hintringer F., Pachinger O. & Roithinger F. X., 2002).

NICE enables an accurate estimation of atrial activation times. This was shown in a recent study (Modre R. et al., 2003) which showed a high correlation between the reconstructed activation time maps (NICE) and a catheter-based electroanatomic maps (CARTO™) in the right atrium during coronary sinus pacing. This finding and the high localization accuracy

during pacing from different clearly defined pacing sites implicate that atrial activation time imaging of focal events is feasible with sufficient spatial and temporal resolution. (Modre R. et al., 2003)

In the work of Berger et al. (Berger T. et al., 2006) noninvasive electrocardiographic imaging of ventricular pre-excitation was performed in the clinical setting of a catheter laboratory. The results obtained by NICE were validated using invasive 3-D electroanatomic mapping of patients with WPW syndrome. The results showed a strong concordance between the reconstructed activation sequences and the anatomical localization of the accessory bundle insertion site as assessed by invasive electroanatomic mapping. The ventricular activation maps reconstructed by NICE were obtained within a computation time of a few minutes. Clinically important steps such as signal processing, classification of QRS morphology, target beat selection and baseline correction were performed with a high level of automation. These findings and the sufficient localization accuracy of the ventricular insertion sites of the accessory pathways (as indicated by the similarity of ventricular activation sequences obtained with NICE and CARTO™) during sinus rhythm as well as during adenosine-induced AV nodal block demonstrated that also mapping of focal ventricular events was feasible. (Berger T. et al., 2006)

Radiofrequency catheter ablation has become the standard treatment for patients with symptomatic WPW syndrome and has success rates of well over 90 % (Schilling R. J., 2002). Noninvasive imaging of the ventricular activation sequence is of special interest for catheter ablation treatment of patients with AV accessory pathways. It supports the identification of the location of the insertion site of the accessory pathway, which is the target substrate for ablation, within a few minutes. Therefore, NICE-based electroanatomic mapping helps to decrease procedure duration, to improve ablation outcome, and to prevent potential complications. In contrast to other electroanatomic imaging techniques, NICE enables single-beat electroanatomic mapping, which is crucial for mapping unstable focal arrhythmias.

In a recent study performed in CRT patients (Berger T. et al., 2011) NICE was used for simultaneous imaging of endocardial and epicardial ventricular activation during native sinus rhythm as well as during different ventricular pacing modes for the first time. Due to limitations of current mapping techniques, there are only limited data available about the effects of different pacing modes on biventricular endocardial and epicardial activation in humans (Auricchio A. et al., 2004; Lambiase P. D. et al., 2004). In this study (Berger T. et al., 2011) control patients showed a deterioration of the ventricular activation sequence during RV pacing comparable to the activation sequence of congestive heart failure (CHF) patients with complete LBBB during native sinus rhythm. During RV pacing the septal, as well as the endocardial and epicardial activation times of the left ventricle were markedly delayed as compared to native sinus rhythm. The septal activation sequence changed from left-to-right during native conduction to a right-to-left septal activation pattern which is in accordance to previous data (Rodriguez L. M. et al., 2003). The earliest LV activation was observed close to the septum mimicking the activation pattern of LBBB patients. Moreover, RV pacing resulted in an increase of total RV and LV activation duration. This increase in ventricular activation duration during RV pacing may be due to cell-to-cell coupled propagation of the activation wavefront until connecting to the intrinsic conduction system and spreading via the Purkinje system. In CHF patients the delay between right and left ventricular endocardial

and epicardial activation was significantly prolonged due to complete LBBB as compared to control patients. In CHF patients biventricular pacing did not affect the direction of transseptal activation respectively the timing of the LV septal breakthrough although the RV septal breakthrough was delayed as compared to native sinus rhythm. This indicates that the major effect of CRT is achieved by preceding the left ventricle by stimulation close to the site of latest left ventricular activation rather than affecting propagation via the intrinsic conduction system. Therefore, optimal placement of the left ventricular lead is crucial and stimulation as close as possible to the site of latest left ventricular activation (during native rhythm) should be aimed at. Epicardial pacing at the left lateral wall and simultaneous endocardial pacing at the right ventricular apex during CRT resulted in a significant decrease of LV total activation duration. Interestingly, total activation duration of the right ventricle was not changed during CRT. This study revealed also differences in propagation velocities of the ventricular activation between the CHF and control group. Left ventricular propagation velocities were significantly decreased in CHF patients as compared to control patients. This is in accordance with the results by Rodriguez et al. (Rodriguez L. M. et al., 2003) who found reduced conduction velocities in patients with congestive heart failure. Both CHF and control patients did not show a significant difference in propagation velocities of the right ventricles. This finding may indicate that the underlying substrate of ventricular dyssynchrony was located mainly within the left ventricle in the CHF patients included into our study. This may be different in patients with arrhythmogenic heart disease or hypertrophic cardiomyopathy. (Berger T. et al., 2011)

In conclusion all these findings show that NICE is a promising tool for noninvasive imaging of electroanatomic activation of the heart. The results indicate that NICE can be a valuable tool in clinical routine. Atrial as well as ventricular cardiac electrical activation can be determined with high accuracies.

The major future challenges will be the extension of activation time reconstruction also for midmyocardial structures. Therefore anisotropic cardiac electrical conductivities have to be considered in the forward problem formulation. Additionally, the inverse problem formulation (regularization term) has to be properly adapted. Implementation of scar tissue into the cardiac model is also a topic for future developments to improve this model-based noninvasive imaging technique.

5. References

Auricchio A., Fantoni C., Regoli F., Carbucicchio C., Goette A., Geller C., Kloss M. & Klein H. (2004). Characterization of left ventricular activation in patients with heart failure and left bundle-branch block, *Circulation* 109(9): 1133–1139.

Barbosa C. R. H. (2003). Simulation of a plane wavefront propagating in cardiac tissue using a cellular automata model, *Physics in Medicine and Biology* 48(24): 4151–4164.

Berger T., Fischer G., Pfeifer B., Modre R., Hanser F., Trieb T., Roithinger F. X., Stuehlinger M., Pachinger O., Tilg B. & Hintringer F. (2006). Single-beat noninvasive imaging of cardiac electrophysiology of ventricular pre-excitation, *Journal of the American College of Cardiology* 48(10): 2045–2055.

Berger T., Hanser F., Hintringer F., Poelzl G., Fischer G., Modre R., Tilg B., Pachinger O. & Roithinger F. X. (2005). Effects of cardiac resynchronization therapy on ventricular

repolarization in patients with congestive heart failure, *Journal of Cardiovascular Electrophysiology* 16(6): 611–617.

Berger T., Pfeifer B., Hanser F. F., Hintringer F., Fischer G., Netzer M., Trieb T., Stühlinger M., Dichtl W., Baumgartner C., Pachinger O. & Seger M. (2011). Single-beat noninvasive imaging of ventricular endocardial and epicardial activation in patients undergoing CRT, *PLoS ONE* 6(1).

Bradley C., Pullan A. & Hunter P. (2000). Effects of material properties and geometry on electrocardiographic forward simulations, *Annals of Biomedical Engineering* 28(7): 721–741.

Cleland J. G., Daubert J. C., Erdmann E., Freemantle N., Gras D., Kappenberger L. & Tavazzi L. (2005). The effect of cardiac resynchronization on morbidity and mortality in heart failure, *New England Journal of Medicine* 352(15): 1539–1549.

Engl H. W., Hanke M. & Neubauer A. (1996). *Regularization of Inverse Problems*, Kluwer, Dordrecht.

Fischer G., Hanser F., Pfeifer B., Seger M., Hintermüller C., Modre R., Tilg B., Trieb T., Berger T., Roithinger F. X. & Hintringer F. (2005). A signal processing pipeline for noninvasive imaging of ventricular preexcitation, *Methods of Information in Medicine* 44(4): 508–515.

Fischer G., Pfeifer B., Seger M., Hintermüller C., Hanser F., Modre R., Tilg B., Trieb T., Kremser C., Roithinger F. X. & Hintringer F. (2005). Computationally efficient noninvasive cardiac activation time imaging, *Methods of Information in Medicine* 44(5): 674–686.

Fischer G., Tilg B., Modre R., Hanser F., Messnarz B. & Wach P. (2002). On modeling the wilson terminal in the boundary and finite element method, *IEEE Transactions on Biomedical Engineering* 49(3): 217–224.

Fischer G., Tilg B., Modre R., Huiskamp G. J. M, ., Fetzer J., Rucker W. & Wach P. (2000). A bidomain model based bem-fem coupling formulation for anisotropic cardiac tissue, *Annals of Biomedical Engineering* 28(10): 1229–1243.

Fischer G., Tilg B., Wach P., Modre R., Leder U. & Nowak K. (1999). Application of high-order boundary elements to the electrocardiographic inverse problem, *Computer Methods and Programs in Biomedicine* 58(2): 119–131.

Geselowitz D. B. (1967). *On bioelectric potentials in inhomogeneous volume conductor*, The Art of Computer Programming, Biophysics Journal.

Geselowitz D. B. & Miller 3rd W. T. (1983). A bidomain model for anisotropic cardiac muscle, *Annals of Biomedical Engineering* 11(3–4): 191–206.

Greensite F. & Huiskamp G. (1998). An improved method for estimating epicardial potentials from the body surface, *IEEE Transactions on Biomedical Engineering* 45(1): 98–104.

Gulrajani R. M. (1988). Models of the electrical activity of the heart and computer simulation of the electrocardiogram, *Critical Reviews in Biomedical Engineering* 16(1): 1–66.

Gulrajani R. M. & Mailloux G. E. (1983). A simulation study of the effects of torso inhomogeneities on electrocardiographic potentials, using realistic heart and torso models, *Circulation Research* 52(1): 45–56.

Hansen P. C. (2001). *Computational Inverse Problems in Electrocardiography*, WIT Press, Southampton, chapter The L-curve and its use in the numerical treatment of inverse problems, pp. 119–142.

He B., Li G. & Zhang X. (2002). Noninvasive three-dimensional activation time imaging of ventricular excitation by means of a heart-excitation model, *Physics in Medicine and Biology* 47(22): 4063–4078.

Hintermüller C., Fischer G., Seger M., Pfeifer B., Hanser F., Modre R. & B., T. (2004). Multi-lead ECG electrode array for clinical application of electrocardiographic inverse problem, *Annual International Conference of the IEEE Engineering in Medicine and Biology Society. IEEE Engineering in Medicine and Biology Society*, Vol. 3, San Francisco, USA, pp. 1941–1944.

Huiskamp G. & Greensite F. (1997). A new method for myocardial activation imaging, *IEEE Transactions on Biomedical Engineering* 44(6): 433–446.

Huiskamp G. J. (1991). Difference formulas for the surface laplacian on a triangulated surface, *Journal of Computational Physics* 95(2): 477–496.

Johnson J. R. (1997). Computational and numerical methods for bioelectric field problems, *Critical Reviews in Biomedical Engineering* 25(1): 1–81.

Klepfer R. N., Johnson C. R. & Macleod R. S. (1997). The effects of inhomogeneities and anisotropies on electrocardiographic fields: a 3-D finite-element study, *IEEE Transactions on Biomedical Engineering* 44(8): 706–719.

Lambiase P. D., Rinaldi A., Hauck J., Mobb M., Elliott D., Mohammad S., Gill J. S. & Bucknall C. A. (2004). Non-contact left ventricular endocardial mapping in cardiac resynchronisation therapy, *Heart* 90(1): 44–51.

Malmivuo J. & Plonsey R. (1995). *Bioelectromagnetism*, Oxford University Press, Oxford.

Messnarz B., Seger M., Modre R., Fischer G., Hanser F. & Tilg B. (2004). A comparison of noninvasive reconstruction of epicardial versus transmembrane potentials in consideration of the null space, *IEEE Transactions on Biomedical Engineering* 51(9): 1609–1618.

Messnarz B., Tilg B., Modre R., Fischer G. & Hanser F. (2004). A new spatiotemporal regularization approach for reconstruction of cardiac transmembrane potential patterns, *IEEE Transactions on Biomedical Engineering* 51(2): 273–281.

Modre R., Seger M., Fischer G., Hintermüller C., P., Hanser F. & Tilg B. (2006). Cardiac anisotropy: Is it negligible regarding noninvasive activation time imaging?, *IEEE Transactions on Biomedical Engineering* 53(4): 569–580.

Modre R., Tilg B., Fischer G., Hanser F., Messnarz B., Seger M., Hintringer F. & Roithinger F. X. (2004). Ventricular surface activation time imaging from electrocardiogram mapping data, *Medical and Biological Engineering and Computing* 42(2): 146–150.

Modre R., Tilg B., Fischer G., Hanser F., Messnarz B., Seger M., Schocke M., Berger T., Hintringer F. & Roithinger F. X. (2003). Atrial noninvasive activation time imaging of paced rhythm data, *Journal of Cardiovascular Electrophysiology* 14(7): 712–719.

Modre R., Tilg B., Fischer G. & Wach P. (2001). An iterative algorithm for myocardial activation time imaging, *Computer Methods and Programs in Biomedicine* 64(1): 1–7.

Modre R., Tilg B., Fischer G. & Wach P. (2002). Noninvasive myocardial activation time imaging: A novel inverse algorithm applied to clinical ECG mapping data, *IEEE Transactions on Biomedical Engineering* 49(10): 1153–1161.

Morady F. (1999). Radio-frequency ablation as treatment for cardiac arrhythmias, *New England Journal of Medicine* 340(7): 534–544.

Pfeifer B., Hanser F., Hintermüller C., Modre - Osprian R., Fischer G., Seger M., Mühlthaler H., Trieb T. & Tilg B. (2005). C++ framework for creating tissue specific segmentation pipelines, *Medical Imaging: Visualization, Image-Guided Procedures, and Display. Proceedings SPIE*, Vol. 5744, San Diego, USA, pp. 317–328.

Pfeifer B., Hanser F., Seger M., Fischer G., Modre-Osprian R. & Tilg B. (2008). Patient-specific volume conductor modeling for Non-Invasive Imaging of Cardiac Electrophysiology, *Open Medical Informatics Journal* 2: 32–41.

Pfeifer B., Seger M., Hintermüller C., Fischer G., Hanser F., Modre R., Mühlthaler H. & Tilg B. (2006). Semiautomatic volume conductor modeling pipeline for imaging the cardiac electrophysiology noninvasively, *Medical image computing and computer-assisted intervention: MICCAI ... International Conference on Medical Image Computing and Computer-Assisted Intervention*, Vol. 9 (Pt 1), Copenhagen, Denmark, pp. 588–595.

Pfeifer B., Seger M., Hintermüller C., Fischer G., Mühlthaler H., Modre - Osprian R. & Tilg B. (2007). Aam-based segmentation for imaging cardiac electrophysiology, *Methods of Information in Medicine* 46:III(1): 36–42.

Press W. H., Teukolsky S. A., Vetterling W. T. & Flannery B. P. (2002). *Numerical recipies in C++ the art of scientific computing*, 2nd edn, Cambridge University Press.

Pullan A. J., Cheng L. K., Nash M. A., Bradley C. P. & Paterson D. J. (2001). Noninvasive electrical imaging of the heart: Theory and model development, *Annals of Biomedical Engineering* 29(10): 817–836.

Ramanathan C., Ghanem R. N., Jia P., Ryu K. & Rudy Y. (2004). Noninvasive electrocardiographic imaging for cardiac electrophysiology and arrhythmia, *Nature in Medicine* 10(4): 422–428.

Ramanathan C., Jia P., Ghanem R., Calvetti D. & Rudy Y. (2003). Noninvasive electrocardiographic imaging (ECGI): application of the generalized minimal residual (GMRes) method, *Annals of Biomedical Engineering* 31(8): 981–994.

Renhardt M., Wach P., Dienstl F., Fleischmann P., Killmann R. & Tilg B. (1992). Computersimulation des Elektro- und Magnetokardiogramms bei Ischämie und infarkt, *Biomedizinische Technik/Biomedical Engineering* 37(s1): 36–38.

Rodriguez L. M., Timmermans C., Nabar A., Beatty G. & Wellens H. J. (2003). Variable patterns of septal activation in patients with left bundle branch block and heart failure, *Journal of Cardiovascular Electrophysiology* 14(2): 135–141.

Roth B. J. (1991). Electrical conductivity values used with the bidomain model of cardiac tissue, *IEEE Transactions on Biomedical Engineering* 44(4): 326–328.

Saxberg B. E. & Cohen R. J. (1990). Cellular automata models for reentrant arrhythmias, *Journal of Electrocardiology* 23(Suppl.): 95.

Schilling R. J. (2002). Which patient should be referred to an electrophysiologist: supraventricular tachycardia, *Heart* 87(3): 299–304.

Seger M., Fischer G., Modre R., Messnarz B., Hanser F. & Tilg B. (2005). Lead field computation for the electrocardiographic inverse problem – finite elements versus boundary elements, *Computer Methods and Programs in Biomedicine* 77(3): 241–252.

Seger M., Fischer G., Modre R., Pfeifer B., Hanser F., Hintermüller C., Roithinger F. X., Hintringer F., Trieb T., Schocke M. & Tilg B. (2004). On-line noninvasive localization of accessory pathways in the EP lab, *Medical image computing and computer-assisted*

intervention: MICCAI ... International Conference on Medical Image Computing and Computer-Assisted Intervention, Vol. 2, St. Malo, France, pp. 502–509.

Simmons W. N., Mackey S., He D. S. & Marcus F. I. (1996). Comparison of gold versus platinum electrodes on myocardial lesion size using radiofrequency energy, *Pacing and Clinical Electrophysiology* 19(4): 398–402.

SippensGroenewegen A., Roithinger F. X., Peeters H. A., Linnenbank A. C., van Hemel N. M., Steiner P. R. & Lesh M. D. (1998). Body surface mapping of atrial arrhythmias: atlas of paced p wave integral maps to localize the focal origin of the right atrial tachycardia, *Journal of Electrocardiology* 31(Suppl.): 85–91.

Tilg B., Fischer G., Modre R., Hanser F., Messnarz B., Schocke M., Kremser C., Berger T., Hintringer F. & Roithinger F. X. (2002). Model-based imaging of cardiac electrical excitation in humans, *IEEE Transactions on Medical Imaging* 21(9): 1031–1039.

Tilg B., Hanser F., Modre-Osprian R., Fischer G., Messnarz B., Berger T., Hintringer F., Pachinger O. & Roithinger F. X. (2002). Clinical ECG mapping and imaging of cardiac electrical excitation, *Journal of Electrocardiology* 35(4, part B): 81–87.

Tilg B., Renhardt M., Fleischmann P. & Wach P. (1992). Modellierung der Leitfähigkeitsanisotropie im Herzen zur EKG- und MKG-berechnung, *Biomedizinische Technik/Biomedical Engineering* 37(s1): 33–35.

Wach P., Modre R., Tilg B. & Fischer G. (2001). An iterative linearized optimization technique for non-linear ill-posed problems applied to cardiac activation time imaging, *COMPEL: The International Journal for Computation and Mathematics in Electrical and Electronic Engineering* 20(3): 676–688.

Wach P., Tilg B., Lafer G. & Rucker W. (1997). Magnetic source imaging in the human heart: estimating cardiac electrical sources from simulated and measured magnetocardiogram data, *Medical and Biological Engineering and Computing* 35(3): 157–166.

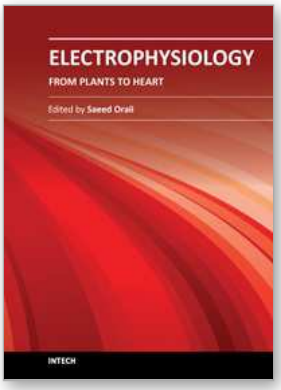

Electrophysiology - From Plants to Heart

Edited by Dr. Saeed Oraii

ISBN 978-953-51-0006-5
Hard cover, 202 pages
Publisher InTech
Published online 03, February, 2012
Published in print edition February, 2012

The outstanding evolution of recording techniques paved the way for better understanding of electrophysiological phenomena within the human organs, including the cardiovascular, ophthalmologic and neural systems. In the field of cardiac electrophysiology, the development of more and more sophisticated recording and mapping techniques made it possible to elucidate the mechanism of various cardiac arrhythmias. This has even led to the evolution of techniques to ablate and cure most complex cardiac arrhythmias. Nevertheless, there is still a long way ahead and this book can be considered a valuable addition to the current knowledge in subjects related to bioelectricity from plants to the human heart.

How to reference

In order to correctly reference this scholarly work, feel free to copy and paste the following:

Michael Seger, Bernhard Pfeifer and Thomas Berger (2012). Noninvasive Imaging of Cardiac Electrophysiology (NICE), Electrophysiology - From Plants to Heart, Dr. Saeed Oraii (Ed.), ISBN: 978-953-51-0006-5, InTech, Available from: http://www.intechopen.com/books/electrophysiology-from-plants-to-heart/nice-noninvasive-imaging-of-cardiac-electrophysiology

INTECH
open science | open minds

InTech Europe
University Campus STeP Ri
Slavka Krautzeka 83/A
51000 Rijeka, Croatia
Phone: +385 (51) 770 447
Fax: +385 (51) 686 166
www.intechopen.com

InTech China
Unit 405, Office Block, Hotel Equatorial Shanghai
No.65, Yan An Road (West), Shanghai, 200040, China
中国上海市延安西路65号上海国际贵都大饭店办公楼405单元
Phone: +86-21-62489820
Fax: +86-21-62489821